Shear-strain mediated magnetoelectric effects revealed by imaging

M. Ghidini[1,2,3*], R. Mansell[4], F. Maccherozzi[2], X. Moya[3], L. C. Phillips[3], W. Yan[3], D. Pesquera[3], C. H. W. Barnes[4], R. P. Cowburn[4], J.-M. Hu[5], S. S. Dhesi[2‡] and N. D. Mathur[3†]

[1] Department of Mathematics, Physics and Computer Science, University of Parma, 43124 Parma, Italy.

[2] Diamond Light Source, Chilton, Didcot, Oxfordshire, OX11 0DE, UK.

[3] Department of Materials Science, University of Cambridge, Cambridge, CB3 0FS, UK.

[4] Cavendish Laboratory, University of Cambridge, CB3 0HE, UK.

[5] Department of Materials Science and Engineering, University of Wisconsin–Madison, Madison, Wisconsin 53706, USA.

* massimo.ghidini@unipr.it

‡ dhesi@diamond.ac.uk

† ndm12@cam.ac.uk

Large changes in the magnetization of ferromagnetic films can be electrically driven by non-180° ferroelectric domain switching in underlying substrates, but the shear components of the strains that mediate these magnetoelectric effects have not been considered so far. Here we reveal the presence of these shear strains in a polycrystalline film of Ni on a $0.68Pb(Mg_{1/3}Nb_{2/3})O_3$-$0.32PbTiO_3$ substrate in the pseudo-cubic $(011)_{pc}$ orientation. Although vibrating sample magnetometry records giant magnetoelectric effects that are consistent with the hitherto expected 90° rotations of a global magnetic easy axis, high-resolution vector maps of magnetization (constructed from photoemission electron microscopy data, with contrast from x-ray magnetic circular dichroism) reveal that the local magnetization typically rotates through smaller angles of 62-84°. This shortfall with respect to 90° is a consequence of the shear strain associated with ferroelectric domain switching. The non-orthogonality represents both a challenge and an opportunity for the development and miniaturization of magnetoelectric devices.

One of the main goals in the study of magnetoelectrics is the electrical control of magnetism[1-5]. This has been previously demonstrated using bulk multiferroic materials[6-10]; strained multiferroic composites[11] or multilayers[12]; ferromagnetic films in which a gate controls semiconductor carrier density[13-16] or interfacial electronic structure[17-19]; ferromagnetic films to which a magnetoelectric (ME) material imparts exchange bias[20]; and ferromagnetic films to which a ferroelectric material imparts strain[21-35], charge[36-39] and/or exchange bias[37-39]. Proposals for electric-write magnetic-read data-storage devices[40-42] focus on patterned ferromagnetic films that experience strain or exchange bias from ferroelectrics that are typically rhombohedral, notably $(1-x)Pb(Mg_{1/3}Nb_{2/3})O_3-xPbTiO_3$ with $x \sim 0.3$ (PMN-PT) and $BiFeO_3$. Here we will focus on strain-mediated coupling because its long-range nature permits ferromagnetic films to be addressed away from the active interface, but the hidden complexity that we reveal in PMN-PT should be relevant for ME studies based on $BiFeO_3$ and other rhombohedral ferroelectrics.

Large strain-mediated ME effects can be achieved using single-crystal substrates of tetragonal $BaTiO_3$ because the electrically driven ferroelectric domain switching yields large and discontinuous changes of strain[21,24,27,30,31], but there is typically a high probability of mechanical failure[43]. By contrast, giant piezoelectric effects[44] can be repeatably driven in single crystals of PMN-PT, as the inherent chemical disorder renders the ferroelectric domains as small as[45] ~300 nm. Therefore PMN-PT is widely exploited in ME heterostructures[22,26,28,29,32,34,35,46,47], and more generally in commercial electromechanical devices such as transducers and actuators.

For ME heterostructures based on PMN-PT, whose polarization lies locally along a pseudocubic $<111>_{pc}$ direction, early studies[22] tended to exploit the $(001)_{pc}$ orientation. If an electrically driven reversal of the out-of-plane polarization component is accompanied by an appropriate change of in-plane polarization (109° switching) then the resulting in-plane strain permits non-volatile ME effects to be achieved. However, it is more common to observe 71° switching[28], where the out-of-plane component of polarization undergoes reversal while the in-plane component does not switch. This type of switching produces discontinuous changes of strain at the coercive field of PMN-PT ('butterfly' curve), but non-volatile ME effects are precluded because the strain at zero electric field is single-valued.

Recent work[26,33,48,49,50] with ME heterostructures based on PMN-PT has instead tended to exploit the $(011)_{pc}$ orientation (Fig. 1). If the PMN-PT polarization possesses an out-of-plane component that is electrically reversed then the in-plane component is either unchanged or reversed, implying

no net change of in-plane strain, such that non-volatile ME effects are precluded. However, if the out-of-plane component of polarization is electrically switched on and off then the in-plane component is necessarily modified (71° and 109° switching), such that the resulting change of in-plane strain permits non-volatile ME effects[25,26]. In practice, the global magnetic easy axis has been reported to undergo electrically driven 90° rotations[25,26,29,35,47,49,51], consistent with a dominant component of normal strain along $y \parallel [0\bar{1}1]_c$ (ref. 48). Given that XMCD-PEEM images of a single magnetization component have likewise been used to infer that the local magnetization undergoes electrically driven rotations of 90° (refs 29,35), no discrepancy between macroscopic and microscopic ME effects has been hitherto identified in the literature, implying that device performance would not be modified by the miniaturization required for data-storage applications[40-42] (PEEM is photoemission electron microscopy, XMCD is x-ray magnetic circular dichroism).

Here we report global and local ME effects in a 10 nm-thick polycrystalline film of Ni on a substrate of PMN-PT ($x = 0.32$) $(011)_{pc}$, whose ferroelectric domains possessed out-of-plane components of polarization that were electrically switched on and off. The global ME effects were measured using a vibrating sample magnetometer, and the local ME effects were identified from high-resolution vector maps of magnetization derived from XMCD-PEEM images. First we show that our macroscopic and microscopic results can easily be misinterpreted to imply that the local magnetization underwent 90° rotations. Then we compare our vector maps on a pixel-by-pixel basis to show that these rotations fell distinctly short of 90°. Our analysis reveals that this shortfall arose because the ferroelectric domain switching was accompanied by shear strains, whose magnitude we identify from the PMN-PT unit cell given in ref. 52. Surprisingly, it would appear that shear strains associated with ferroelectric domain switching have been hitherto neglected, although it is well known that shear strains can arise via the continuous piezoelectric effect with no ferroelectric domain switching[53]. The positive and negative shear strains that we identify in ferroelectric domains as small as[45] ~300 nm would be extremely challenging to measure directly with x-ray diffraction[48]. By contrast, the high-resolution images of our magnetically soft magnetostrictive film serve as a very sensitive strain gauge. The shear strains associated with rhombohedral ferroelectric domain switching should in future be taken into account when designing ME memory, especially because we will show that these shear strains permit data to be written both electrically and magnetically.

Macroscopic and microscopic magnetoelectric effects

All data presented in the main paper were obtained from a single sample, whose fabrication and history are described in Methods. The electrically virgin sample possessed no in-plane magnetic anisotropy (Supplementary Note 1) because the unoriented grains in the Ni film precluded a net magnetocrystalline anisotropy, and because the unoriented domains in the PMN-PT substrate precluded a net stress anisotropy[27] (macroscopic magnetic measurements are described in Methods). Poling the substrate by applying and removing an electric field of $E = -1$ MV m^{-1} along $+z$ (Fig. 1) created in our negative-magnetostriction film a non-volatile uniaxial magnetic anisotropy along y, and the magnitude of this anisotropy implies a y-axis compressive strain of 0.08% consistent with ref. 26 (Supplementary Note 1). On subsequently cycling the electric field at magnetic remanence, we found minima of y-axis magnetization M_y (Fig. 2a) and maxima of x-axis magnetization M_x (Supplementary Note 2) near the ± 0.37 MV m^{-1} coercive field (Fig. S4a, Supplementary Note 3) at which ferroelectric domain polarizations are understood to switch in-plane ($P_{3,4}^{\pm}$, Fig. 1). These extrema in magnetization are consistent with the expected[25] extrema in macroscopic strain (Fig. S4b, Supplementary Note 3), which have been hitherto understood to drive 90° rotations of a global magnetic easy axis[25,26,29,35,47,49,51]. The minima in M_y correspond to a ~50% change of magnetization, and a peak ME coupling coefficient of $\alpha_y = \mu_0 \mathrm{d}M_y/\mathrm{d}E \sim 1.6 \times 10^{-6}$ s m^{-1} (Fig. 2b).

Magnetic hysteresis loops that were measured along orthogonal in-plane directions at fields of $E_1 = 0$ (Fig. 3a), $E_2 = +0.167$ MV m^{-1} (Fig. 3d) and $E_3 = +1$ MV m^{-1} (Fig. 3g) are also consistent with the hitherto expected 90° rotation of a global easy axis[25,26,29,35,47,49,51] created by poling. This is because both the first ($E_1 \rightarrow E_2$) and second ($E_2 \rightarrow E_3$) field steps appear to interconvert the hard and easy directions, as seen more clearly by comparing polar plots of magnetic-hysteresis-loop squareness at each electric field (blue data, Fig. 3c,f,i). However, we will see below that local ME measurements, and calculations based on unit-cell distortions, reveal that the switched state at E_2 involves two misaligned uniaxial magnetic anisotropies rather than a single easy axis.

In order to investigate local ME effects in the same sample, we used XMCD-PEEM to obtain high-resolution vector maps (see Methods) of the in-plane magnetization direction ϕ at E_1, E_2 and E_3 (Fig. 3b,e,h). At E_1 (Fig. 3b) and E_3 (Fig. 3h), the 50 μm-diameter field of view contained a small number of large domains, whose magnetizations lay approximately along $\pm y$. For the intervening state at E_2 (Fig. 3e), the same field of view contained a large number of small domains, whose magnetizations appear to have lain approximately along $\pm x$ (except for a few regions that did

not switch). However, the angular resolution of the colour wheel is insufficient for visual inspection to confirm that the local magnetization typically rotated by the 90° that one would expect from our macroscopic measurements (blue data, Fig. 3c,f,i), previous macroscopic measurements[25,26,29,35,47,49,51], and previous microscopic measurements[29,35]. Plotting the pixel magnetization directions in our vector maps on polar plots (red data, Fig. 3c,f,i) also gives the superficial impression that each electric-field step typically rotated the local magnetization by roughly the hitherto expected[25,26,29,35,47,49,51] value of 90°. However, at E_1 and E_3 there are two slim lobes, whereas the structure of the polar plot at E_2 is more complex. This observation inspires the following pixel-by-pixel comparison of our vector maps.

Pixel-by-pixel comparison

The changes of magnetization direction $\Delta\phi$ are mapped for both $E_1 \rightarrow E_2$ (Fig. 4a) and $E_2 \rightarrow E_3$ (Fig. 4e), after excluding the small (white) areas between magnetic domain walls in the vector maps at E_1 (Fig. 3b) and E_3 (Fig. 3h), such that we consider only regions where the magnetization returned to its original direction. The number N' of unexcluded green pixels in our vector map at E_1 that underwent magnetization direction change $\Delta\phi$ during $E_1 \rightarrow E_2$ is plotted in Fig. 4b, while the number N' of unexcluded purple pixels in our vector map at E_1 that underwent magnetization direction change $\Delta\phi$ during $E_1 \rightarrow E_2$ is plotted in Fig. 4c. Similarly, the number N' of unexcluded green pixels in our vector map at E_3 that resulted from magnetization direction change $\Delta\phi$ during $E_2 \rightarrow E_3$ is plotted in Fig. 4f, while the number N' of unexcluded purple pixels in our vector map at E_3 that resulted from magnetization direction change $\Delta\phi$ during $E_2 \rightarrow E_3$ is plotted in Fig. 4g. Having thus considered separately each type of magnetic domain (unexcluded green and purple pixels) in our vector maps at E_1 and E_3, we see that the magnetization of many pixels switched by large angles $\Delta\phi$ that typically fall well short of the hitherto expected[25,26,29,35,47,49,51] value of 90° (Fig. 4b,c,f,g).

Given that the two FWHM peaks in Fig. 4b (in Fig. 4c) are essentially interchanged in Fig. 4f (in Fig. 4g), we infer that the net effect of the two field steps was to switch and switch back the magnetization of many pixels by large angles of typically less than 90°. To identify which pixels switched and switched back in this way, we filtered our maps of $\Delta\phi$ (Fig. 4a,e) using the colour code in $N'(\Delta\phi)$ (Fig. 4b,c,f,g) to produce simplified maps of $\Delta\phi$ (Fig. 4d,h). Comparison of the two simplified maps confirms that the magnetization of many pixels switched and switched back by

large angles of typically less than 90° (yellow, Fig. 4i). These regions are either purple in Fig. 4d and green in Fig. 4h, or else they are green in Fig. 4d and blue/purple in Fig. 4h.

Having used our formal pixel-by-pixel comparison (Fig. 4) to reveal that the magnetization of many pixels switched and switched back by large angles of typically less than 90°, we will now investigate whether this sub-90° switching could have been directly identified from our vector maps (Fig. 3b,e,h) and polar plots (red data, Fig. 3c,f,i). In our vector maps, pixels coloured purple at E_1 and E_3 were typically red/blue at E_2, while pixels coloured green at E_1 and E_3 were typically orange/cyan at E_2, thus confirming the sub-90° nature of the switching. By splitting our polar plot at E_2 (Fig. 3f) in order to distinguish pixels that were green at both E_1 and E_3 (brown data appearing in both Fig. 5a,b) from pixels that were purple at both E_1 and E_3 (black data appearing in both Fig. 5a,b), the predominance of four magnetization directions at E_2 (lobes in the brown and black data, Fig. 5a,b) likewise confirms the sub-90° nature of the switching. All polar plots in Fig. 5 exclude the pixels between the magnetic domain walls in our vector maps at E_1 and E_3. Fig. 5a compares the split polar plot at E_2 with the polar plot at E_1 (pink), and Fig. 5b compares the split polar plot at E_2 with the polar plot at E_3 (pink). Fig. 5a,b also show the modal changes of magnetization for unexcluded pixels (Fig. 4b,c,f,g), thus summarizing the key results from Figs 3,4.

The role of shear strain

The changes of local magnetization in our Ni film are typically less than 90° because ferroelectric domain switching in rhombohedral PMN-PT generates not just the well known normal strains, but also shear strains that have surprisingly been hitherto unappreciated. We will now quantify the expected magnetic changes by investigating the distortions of the unit cell that arose when the polarization switched in and out of the x-y plane lying parallel to the $(011)_{pc}$ surface of the substrate.

The effect of ferroelectric domain switching on quadrants of the pseudocubic unit cell ($a = 4.017$ Å, $\theta = 89.89°$)[52] for rhombohedral PMN-PT is calculated in Supplementary Note 4, and schematised in Fig. 6a-e, assuming for simplicity an idealised scenario that neglects strain between ferroelectric domains. When the polarization lay away from the plane of a given quadrant, the quadrant was undistorted (green, Fig. 6a-e). By contrast, when the polarization switched into the plane of a given quadrant, this quadrant developed the as-calculated shear strain of ±0.14% in addition to the as-calculated normal strain of +0.19% (blue and orange, Fig. 6a-e). As shown in Supplementary Note 5, these shear and normal strains may be transformed into orthogonal normal strains (-0.07%

and +0.26%) by rotating the basis through $\mp 27.4°$ in the plane to which the polarization had switched, such that polarization switching into the *x-y* plane at E_2 created magnetic easy axes in the film at the complementary angles of ±62.6° to *y* (non-vertical grey arrows, Fig. 6f). Specifically, regions of the film that switched with positive shear strain (due to the formation of $P_3^\pm$ domains, left panel in Fig. 6d) developed easy axes at +62.6° to *y*, while regions of the film that switched with negative shear strain (due to the formation of $P_4^\pm$ domains, right panel in Fig. 6d) developed easy axes at -62.6° to *y*. The creation and subsequent destruction of these easy axes at ±62.6° to *y* explains the sub-90° magnetic switching that we identified as our key finding via XMCD-PEEM vector maps. A full explanation of our magnetic vector maps appears in Supplementary Note 6.

The misaligned magnetic easy axes at E_2, which lie in spatially distinct regions as explained above, are directly evidenced by the paired modal switching angles in Fig. 4b,c,f,g (where ferroelectric domain populations determine peak magnitudes). The two modal angles of 62° and -64° approximately match our predicted values of ±62.6°, while six modal angles adopt larger values. Departures from the predicted values are attributed to strain-mediated interactions between the many ferroelectric domains that are present at all fields, and the prevalence of large-angle switching implies that these interactions tend to suppress the shear strains of interest (because the limiting case of normal strain ε_{yy} with no shear strain ε_{xy} would favour the hitherto expected[25,26,29,35,47,49,51] rotations of 90°). Note that the misaligned magnetic easy axes at E_2 are not apparent from our macroscopic measurements (blue data, Fig. 3f) because the sum of the projections of these nearby easy axes is larger along the bisecting *x* axis than it is along either one of these easy axes themselves, such that macroscopic measurements misleadingly imply a single magnetic easy axis along *x*.

The macroscopic ME effects that we report would be larger if the local magnetization were to rotate by 90° in the absence of any shear. Despite this, our peak ME coupling coefficient ($\alpha_y \sim 1.6 \times 10^{-6}$ s m^{-1}, Fig. 2b) is larger than the large values that were achieved without shear using BaTiO$_3$ substrates with epitaxial films of either La$_{0.67}$Sr$_{0.33}$MnO$_3$ (2.3×10^{-7} s m^{-1}, ref. 21) or FeRh (1.4×10^{-6} s m^{-1}, ref. 30) (ref. 30 presents 1.4×10^{-6} s m^{-1} in Fig. 3a, and reports 1.6×10^{-5} s m^{-1} for a virgin effect measured indirectly while sweeping temperature). We attribute our large ME coupling coefficient to two factors, namely the use of a substrate in which ferroelectric domain switching produces large changes of strain[44], and the use of a magnetically soft magnetostrictive film with no in-plane anisotropy prior to poling (Supplementary Note 1). For completeness, note that our peak

ME coupling coefficient is similar to a prediction[54] of 1.86×10^{-6} s m^{-1} for epitaxial Ni on a ferroelectric substrate whose piezoelectric response was parameterized without ferroelectric domain switching.

Outlook

Our observation that electrically driven shear strain is responsible for sub-90° magnetic switching has immediate implications for the performance of ME random access memory (MERAM) devices, where a soft ferromagnet is coupled by strain and/or exchange to a weakly clamped rhombohedral ferroelectric such as PMN-PT, PZN-PT, Zr-rich $PbZr_xTi_{1-x}O_3$ (PZT), or $BiFeO_3$. Most notably, by avoiding the hitherto expected[25,26,29,35,47,49,51] magnetic switching angle of 90°, one guarantees a deterministic return to the initial magnetization direction with no possibility of magnetization reversal. This deterministic switching offers the prospect of writing data both magnetically and electrically, as originally envisaged for multiferroic materials[2] and discussed below.

As seen from Fig. 6f, the uniform magnetization in a small dot could be magnetically switched in order to store non-volatile binary information via the sign of M_y (three possible states with $M_y > 0$, three possible states with $M_y < 0$). It could also be electrically switched in order to independently store non-volatile binary information via the magnitude of M_y (two possible states with large $|M_y|$, four possible states with small $|M_y|$). This magnetically and electrically driven switching could be independently detected in the free layer of a magnetic tunnel junction via device resistance, as envisaged for MERAM devices displaying electrically driven magnetization reversal[38,40-42]. Our proposed readout scheme would be insensitive to the sign of M_x, and therefore insensitive to the sign of the shear strain, implying that the in-plane component of dot polarization need not remain uniform (in contrast with the need for a uniform out-of-plane component).

In summary, we have employed a pixel-by-pixel comparison of high-resolution vector magnetization maps in order to reveal that rotations of the local magnetization typically fell short of 90° when a 10 nm-thick Ni film experienced strain from ferroelectric domain switching in a rhombohedral PMN-PT (011)$_{pc}$ substrate. This angular shortfall arose as a consequence of hitherto unappreciated shear-strain components that were switched on (off) by electrically switching off (on) the out-of-plane component of electrical polarization in a given ferroelectric domain. Nevertheless, our macroscopically measured ME effects exceed the best values on record[21,30]. In future, ME effects mediated by shear-strain components could be exploited to realize nanoscale devices that independently store electrically and magnetically written data. More generally, the shear strains that

we have identified in our multiferroic heterostructure represents a new twist in the study of ME effects, thus echoing the 'magnetic twist for ferroelectricity' that was coined elsewhere in the context of multiferroic materials[4].

Author contributions

M.G. initiated the study. M.G. and N.D.M. led the project with S.S.D. R.M., R.P.C. and C.H.W.B. were responsible for the growth of thin film Ni. The collection and preliminary analysis of PEEM data were performed by M.G., with assistance from X.M., L.C.P and W.Y. All other experimental work was performed by M.G. F.M. and S.S.D. were responsible for constructing PEEM vector maps, and the subsequent pixel by pixel analysis. D.P. performed image and data processing. N.D.M. proposed the pixel-by-pixel analysis of PEEM vector maps that led to the key finding of sub 90° magnetization rotation. J. M.H. identified and calculated the shear strain that accompanies ferroelectric domain switching in PMN-PT. M.G. identified the resulting principal axes of strain and hence magnetic easy axes. M.G. and N.D.M. interpreted the observed magnetoelectric effects. N.D.M wrote the manuscript with M.G., using substantive feedback from S.S.D. and J. M.H., and additional feedback from R.M.

Data Availability

All relevant data are available from the authors on request.

## Competing interests

The authors declare no competing interests.
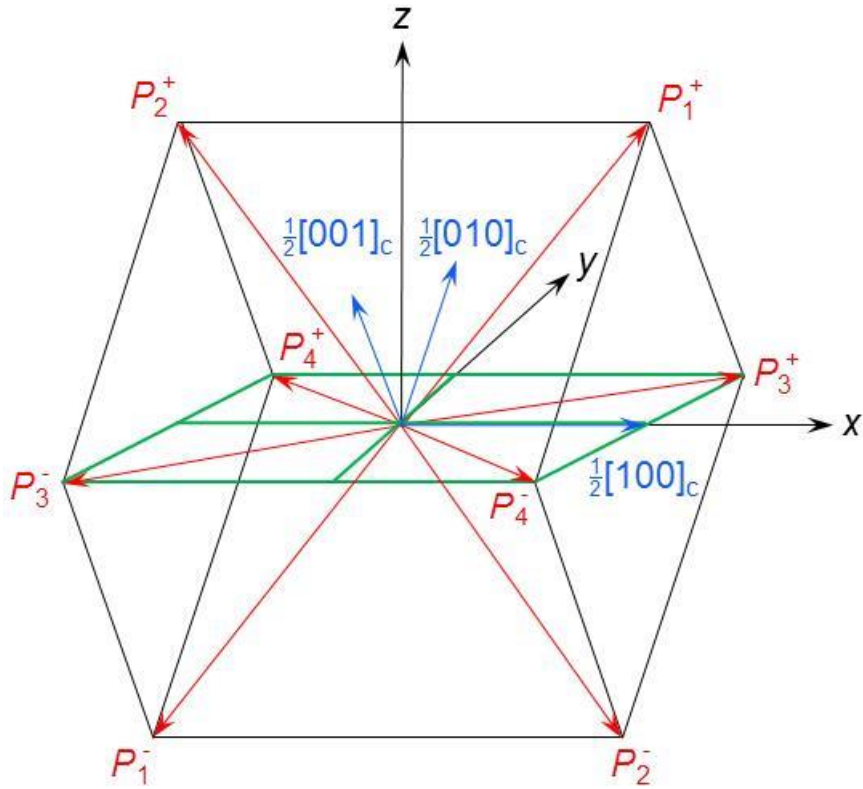
Figure 1. Cubic representation of the pseudocubic PMN-PT (011)$_{pc}$ unit cell. Black arrows denote Cartesian directions $x \parallel [100]_c$, $y \parallel [0\bar{1}1]_c$ and $z \parallel [011]_c$ that lie parallel to the orthogonal substrate edges (c denotes cubic). The x-y plane (containing green unit-cell quadrants) represents the PMN-PT surface on which the Ni film was deposited. The eight $<111>_c$ directions (red arrows) correspond closely to permitted directions of local polarization in the pseudocubic unit cell, but the correspondence is not exact due to the pseudocubic distortion. Numbered directions of polarization P lying antiparallel to each other are identified via + and - subscripts. Cubic basis vectors (blue arrows) correspond closely to the pseudocubic basis vectors (not shown) for polarization $P_1^{\pm}$ only. Switching through 71° (through 109°) implies that a red arrow head traverses a cube edge (face diagonal).
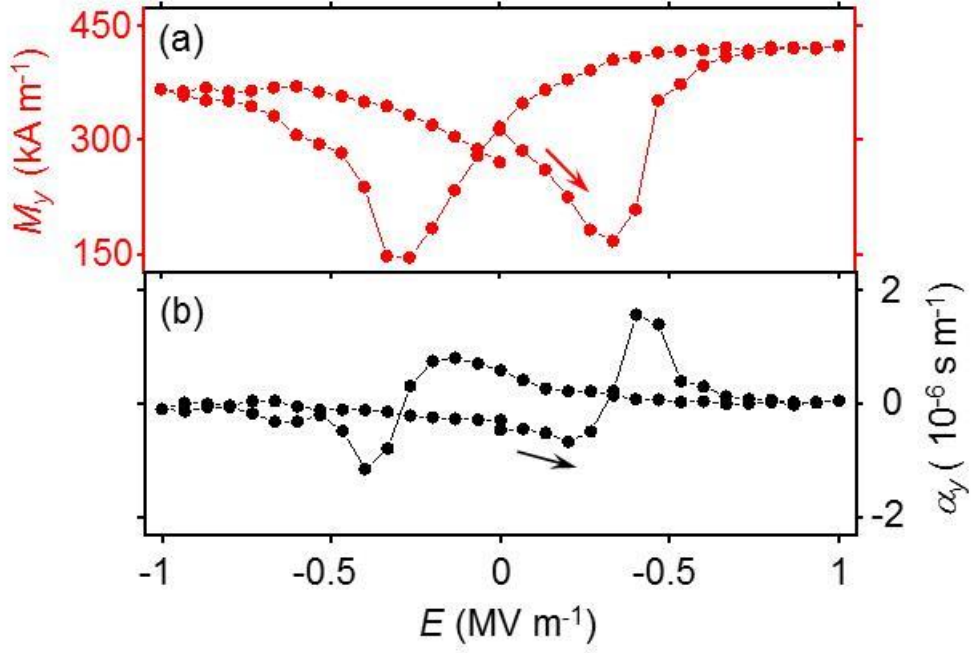
Figure 2. Macroscopic magnetoelectric effects in Ni//PMN-PT (011)$_{pc}$. (a) In-plane magnetization component M_y versus electric field E applied perpendicular to the film plane. Hence (b) ME coupling coefficient $\alpha_y = \mu_0 dM_y/dE$. Immediately prior to data acquisition, a magnetic field of $\mu_0 H = 1$ T was applied and removed along y. Prior to the application of this magnetic field, the sample had experienced many electrical cycles. Arrows identify initial branch. Data recorded on Sample 1.
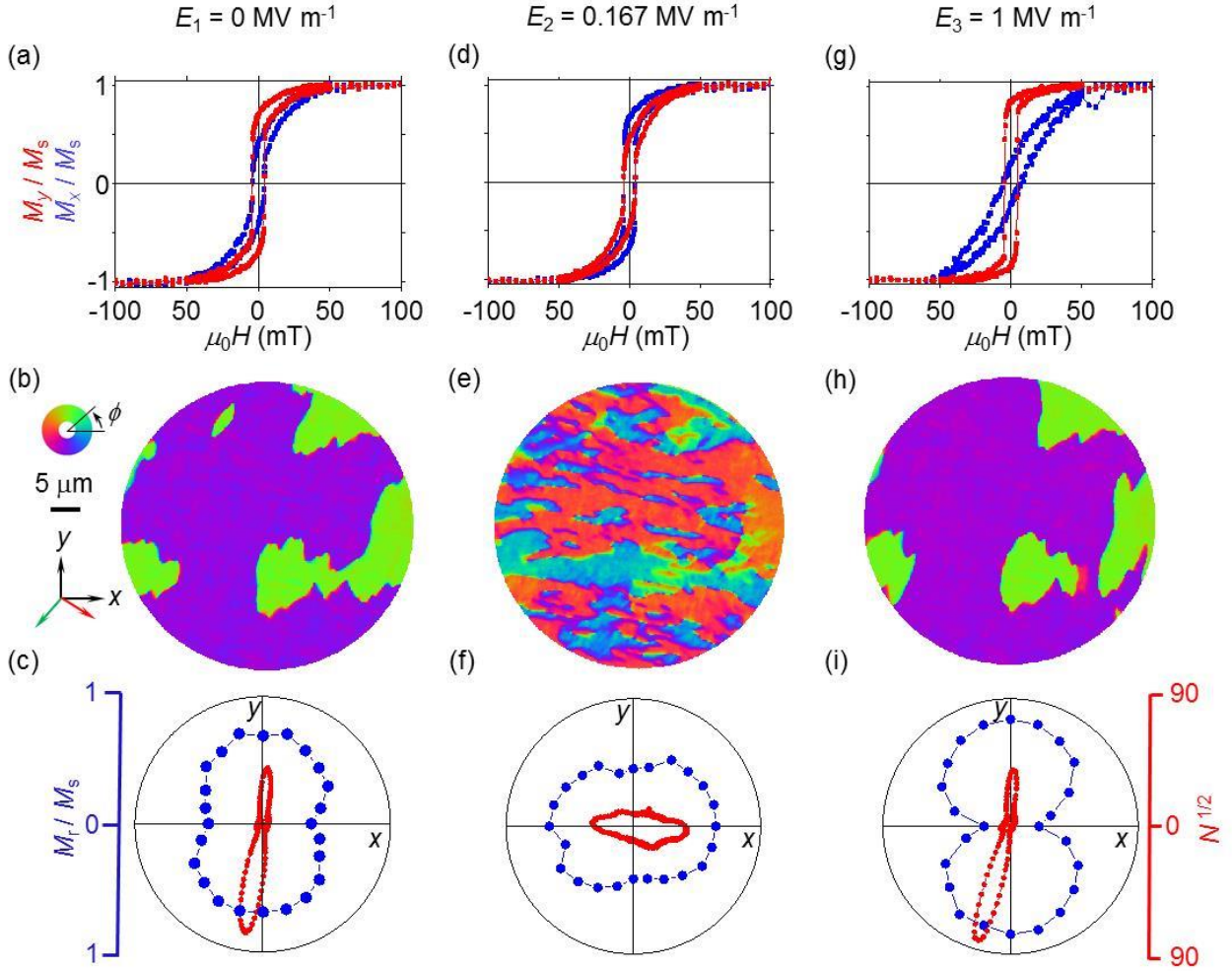
Figure 3. Global and local magnetization for magnetoelectric switching in Ni//PMN-PT (011)$_{pc}$. For electric field (a-c) $E_1 = 0$, (d-f) $E_2 = 0.167$ MV m^{-1} and (g-i) $E_3 = 1$ MV m^{-1}, we show: (a,d,g) reduced magnetization components M_x/M_s (blue) and M_y/M_s (red) versus collinear applied magnetic field H; (b,e,h) 50 μm-diameter magnetic vector maps of in-plane magnetization direction ϕ; and (c,f,i) polar plots of loop squareness M_r/M_s (blue) derived from plots that include those shown in (a,d,g), and polar plots of $N^{1/2}$ (red), where N is the number of pixels in (b,e,h) with magnetization direction ϕ. We use $N^{1/2}$ rather than N, so that the area under the curve in an infinitesimal angular sector is proportional to N rather than N^2. Green and red arrows in (b,e,h) denote the in-plane projections of the grazing-incidence x-ray beam, M_r denotes remanent magnetization, and M_s denotes saturation magnetization. Prior to data acquisition, we poled the sample by applying and removing an electric field of $E = -1$ MV m^{-1}. Twenty bipolar sweeps did not reveal any evidence of fatigue. Data recorded on Sample 1.
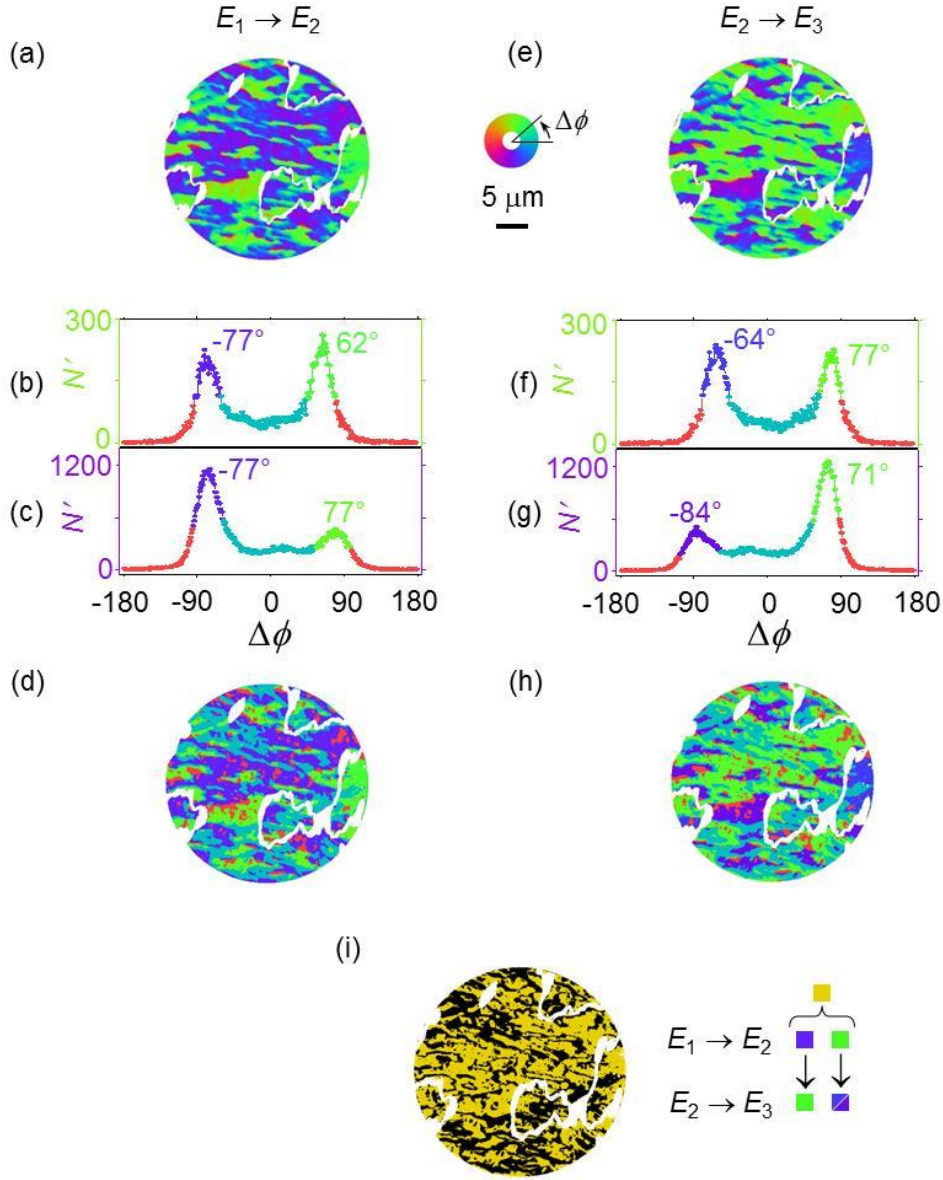
Figure 4. Changes in the local magnetization for magnetoelectric switching in Ni//PMN-PT (011)$_{pc}$. Comparison of the magnetic vector maps in Fig. 3b,e,h for (a-d) $E_1 \rightarrow E_2$ and (e-h) $E_2 \rightarrow E_3$, and (i) comparison of these two field steps. Data between the magnetic domain walls at E_1 and E_3 correspond to the white regions in all five images, and are likewise excluded from the four histograms. (a,e) 50 μm-diameter maps showing changes of pixel magnetization direction $-180° \leq \Delta\phi \leq 180°$. (b,c,f,g) The number of pixels N' that undergo a change of magnetization direction $\Delta\phi$, for pixels that are (b,f) green and (c,g) purple at (b,c) E_1 and (f,g) E_3, with modal angles specified. Data colour represents either a modal angle, 0° or ±180° on the colour wheel in (a,e). (d,h) The maps in (a,e) with the colour filtering shown in (b,c,f,g). (i) Yellow regions represent pixels that are purple in (d) and green in (h), or green in (d) and blue/purple in (h), such that they show where the magnetization switched and switched back within the FWHM peaks of (b,c,f,g). Black regions represent all other coloured regions in (d,h).

13
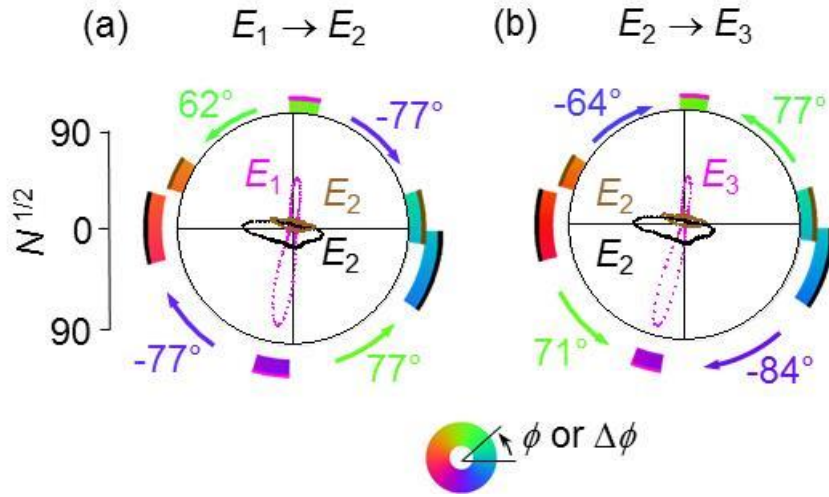
Figure 5. Local magnetization and changes of local magnetization for magnetoelectric switching in Ni//PMN-PT (011)$_{pc}$. (a) $E_1 \rightarrow E_2$ and (b) $E_2 \rightarrow E_3$. We present the polar plots of $N^{1/2}(\phi)$ (Fig. 3c,f,i) at (a) E_1 (pink data) and E_2 (black and brown data), and at (b) E_2 (black and brown data) and E_3 (pink data), after excluding all pixels between magnetic domain walls at E_1 and E_3 (white regions in Fig. 4 images), and after distinguishing at E_2 the pixels that were purple at both E_1 and E_3 (black data) from the pixels that were green at both E_1 and E_3 (brown data). Peripheral outer (inner) arcs identify FWHM intervals for each peak in $N(\phi)$ by data colour (position on the colour wheel). Modal values of $\Delta\phi$ from Fig. 4b,c,f,g are rendered using the colour wheel, like-coloured arrow lengths are arbitrary.
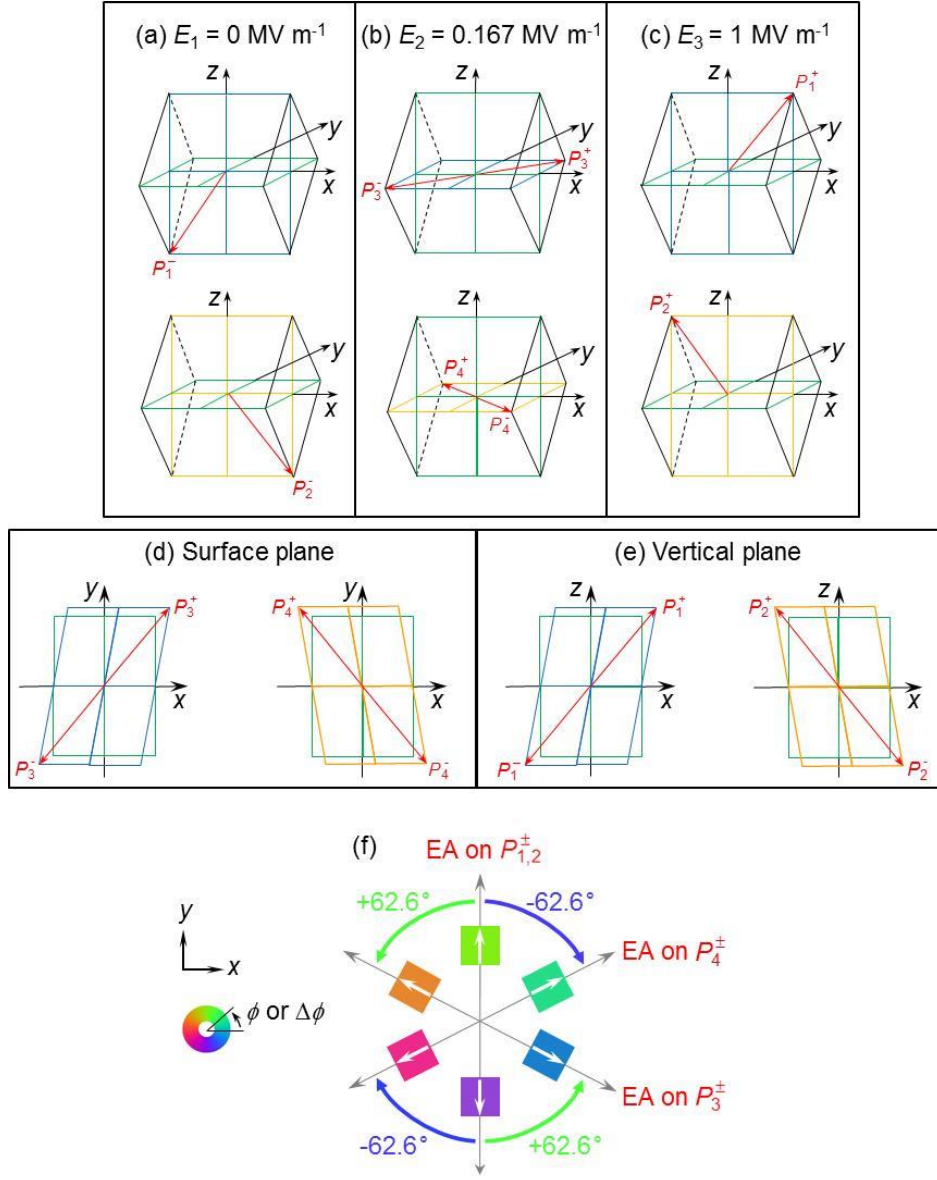
Figure 6. Predicted local magnetoelectric switching for Ni//PMN-PT (011)_pc. (a-c) Cubic representation of the pseudocubic PMN-PT unit cell, showing permitted directions of local polarization (red arrows) at (a) E_1, (b) E_2 and (c) E_3. Unit-cell quadrants possess either no distortion (green), or a distortion (not shown) whose shear component is positive (blue) or negative (orange). These distortions are shown in (d) where we compare distorted quadrants at E_2 with undistorted quadrants at E_1 and E_3, and in (e) where we compare distorted quadrants at E_1 and E_3 with undistorted quadrants at E_2. Quadrant distortions of (d) $\varepsilon_{xy} = \pm0.14\%$ and $\varepsilon_{yy} = 0.19\%$, and (e) $\varepsilon_{xz} = \pm0.14\%$ and $\varepsilon_{zz} = 0.19\%$, and the acute angle of 89.84° for the simple shear shown here, are exaggerated for clarity; $\varepsilon_{xx} = 0$. (f) In the overlying Ni film, strain-induced magnetic easy axes (grey arrows) were created at E_1 and E_3 along y on $P_{1,2}^{\pm}$ domains, and at E_2 at $\pm62.6°$ to y on $P_{3,4}^{\pm}$ domains (EA denotes easy axis). White arrows and coloured squares show the directions of local magnetization ϕ. Changes $\Delta\phi = \pm62.6°$ are shown using coloured arrows.

References

[1] Fiebig, M. Revival of the magnetoelectric effect. *J. Phys. D* **38,** R123-R152 (2005).

[2] Eerenstein, W., Mathur, N. D. & Scott, J. F. Multiferroic and magnetoelectric materials. *Nature* **442,** 759-765 (2006).

[3] Ramesh, R. & Spaldin, N. A. Multiferroics: progress and prospects in thin films. *Nature Materials* **6**, 21-29 (2007).

[4] Cheong, S.-W. & Mostovoy, M. Multiferroics: a magnetic twist for ferroelectricity. *Nature Materials* **6**, 13-20 (2007).

[5] Nan, C.-W., Bichurin, M. I., Dong, S., Viehland, D. & Srinivasan, G. Multiferroic magnetoelectric composites: Historical perspective, status, and future directions. *J. Appl. Phys.* **103**, 031101 (2008).

[6] Lebeugle, D., Colson, D., Forget, A., Viret, M., Bataille, A. M. & Gukasov, A. Electric-Field-Induced Spin Flop in $BiFeO_3$ Single Crystals at Room Temperature. *Phys. Rev. Lett.* **100,** 227602 (2008).

[7] Choi, Y. J., Zhang, C. L., Lee, N. & Cheong, S.-W. Cross-Control of Magnetization and Polarization by Electric and Magnetic Fields with Competing Multiferroic and Weak-Ferromagnetic Phases. *Phys. Rev. Lett.* **105,** 097201 (2010).

[8] Tokunaga, Y., Taguchi, Y., Arima, T. H. & Tokura, Y. Electric-field-induced generation and reversal of ferromagnetic moment in ferrites. *Nature Physics* **8,** 838-844 (2012).

[9] Chun, S. H. et al. Electric Field Control of Nonvolatile Four-State Magnetization at Room Temperature. *Phys. Rev. Lett.* **108,** 177201 (2012).

[10] Chai, Y.-S. et al. Electrical control of large magnetization reversal in a helimagnet. *Nature Communications* **5,** 4208 (2014).

[11] Zavaliche, F. et al. Electrically Assisted Magnetic Recording in Multiferroic Nanostructures. *Nano Letters* **7,** 1586-1590 (2007).

[12] Mundy, J. A. et al. Atomically engineered ferroic layers yield a room-temperature magnetoelectric multiferroic. *Nature* **537,** 523-527 (2016).

[13] Ohno, H. et al. Electric-field control of ferromagnetism. *Nature* **408,** 944-946 (2000).

[14] Chiba, D., Yamanouchi, M., Matsukura, F. & Ohno, H. Electrical Manipulation of Magnetization Reversal in a Ferromagnetic Semiconductor. *Science* **301,** 943-945 (2003).

[15] Chiba, D. et al. Magnetization vector manipulation by electric fields. *Nature* **455,** 515-518 (2008).

[16] Yamada, Y. et al. Electrically Induced Ferromagnetism at Room Temperature in Cobalt-Doped Titanium Dioxide. *Science* **332,** 1065-1067 (2011).

[17] Maruyama, T. et al. Large voltage-induced magnetic anisotropy change in a few atomic layers of iron. *Nature Nanotechnology* **4,** 158-161 (2009).

[18] Endo, M., Kanai, S., Ikeda, S., Matsukura, F. & Ohno, H. Electric-field effects on thickness dependent magnetic anisotropy of sputtered MgO / $Co_{40}Fe_{40}B_{20}$/ Ta structures. *Appl. Phys. Lett.* **96,** 212503 (2010).

[19] Cuellar, F. A. et al. Reversible electric-field control of magnetization at oxide interfaces. *Nature Communications* **5**, 4215- 4222 (2014).

[20] Borisov, P., Hochstrat, A., Chen, X., Kleemann, W. & Binek, C. Magnetoelectric Switching of Exchange Bias. *Phys. Rev. Lett.* **94**, 117203 (2005).

[21] Eerenstein, W., Wiora, M., Prieto, J. L., Scott, J. F. & Mathur, N. D. Giant sharp and persistent converse magnetoelectric effects in multiferroic epitaxial heterostructures. *Nat. Mater.* **6**, 348–351 (2007).

[22] Thiele, C., Dörr, K., Bilani, O., Rödel, J. & Schultz, L. Influence of strain on the magnetization and magnetoelectric effect in $La_{0.7}A_{0.3}MnO_3$/PMN-PT(001) (*A*=Sr, Ca). *Phys. Rev. B* **75**, 054408 (2007).

[23] Sahoo, S. et al. Ferroelectric control of magnetism in $BaTiO_3$ /Fe heterostructures via interface strain coupling. *Phys. Rev. B* **76,** 092108 (2007).

[24] Geprägs, S., Brandlmaier, A., Opel, M., Gross, R. & Goennenwein, S. T. B. Electric field controlled manipulation of the magnetization in $Ni/BaTiO_3$ hybrid structures. *Appl. Phys. Lett.* **96,** 142509 (2010).

[25] Wu, T. et al. Giant electric-field-induced reversible and permanent magnetization reorientation on magnetoelectric $Ni/(011)[PbMg_{1/3}Nb_{2/3}O_3]_{(1-x)}–[PbTiO_3]_x$ *Appl. Phys. Lett.* **98,** 012504 (2011).

[26] Wu, T. et al. Electrical control of reversible and permanent magnetization reorientation for magnetoelectric memory devices. *Appl. Phys. Lett*. **98,** 262504 (2011).

[27] Lahtinen, T. H. E., Franke, K. J. A. & van Dijken, S. Electric-field control of magnetic domain wall motion and local magnetization reversal. *Scientific Reports* **2,** 258-263 (2012).

[28] Zhang, S. et al. Electric-Field Control of Nonvolatile Magnetization in $Co_{40}Fe_{40}B_{20}/(PbMg_{1/3}Nb_{2/3})_{0.7}Ti_{0.3}O_3$ Structure at Room Temperature. *Phys. Rev. Lett.* **108,** 137203 (2012).

[29] Buzzi, M. et al. Single Domain Spin Manipulation by Electric Fields in Strain Coupled Artificial Multiferroic Nanostructures. *Phys. Rev. Lett.* **111,** 027204 (2013).

[30] Cherifi, R. O. et al. Electric-field control of magnetic order above room temperature. *Nature Materials* **13,** 345-351 (2014).

[31] M. Ghidini et al. Perpendicular Local Magnetization Under Voltage Control in Ni Films on Ferroelectric BaTiO$_3$ Substrates. *Adv. Mater.* **27,** 1460-1465 (2015).

[32] Chopdekar, R. V. et al. Giant reversible anisotropy changes at room temperature in a (La,Sr)MnO$_3$/Pb(Mg,Nb,Ti)O$_3$ magneto-electric heterostructure. *Sci. Rep.* **6**, 27501 (2016).

[33] Gao, Y. et al. Dynamic in situ observation of voltage-driven repeatable magnetization reversal at room temperature. *Sci. Rep.* **6,** 23696 (2016).

[34] Li, P. et al. Spatially Resolved Ferroelectric Domain-Switching-Controlled Magnetism in Co$_{40}$Fe$_{40}$B$_{20}$/Pb(Mg$_{1/3}$Nb$_{2/3}$)$_{0.7}$Ti$_{0.3}$O$_3$ Multiferroic Heterostructure. *ACS Appl. Mater. Interfaces*, **9,** 2642-2649 (2017).

[35] Lo Conte, R. et al. Influence of Nonuniform Micron-Scale Strain Distributions on the Electrical Reorientation of Magnetic Microstructures in a Composite Multiferroic Heterostructure. *Nano Lett.* **18,** 1952-1961 (2018).

[36] Molegraaf, H. J. A. et al. Magnetoelectric Effects in Complex Oxides with Competing Ground States. *Adv. Mater.* **21,** 3470-3474 (2009).

[37] Skumryev, V. et al. Magnetization Reversal by Electric-Field Decoupling of Magnetic and Ferroelectric Domain Walls in Multiferroic-Based Heterostructures. *Phys. Rev. Lett.* **106,** 057206 (2011).

[38] Heron, J. T. et al. Deterministic switching of ferromagnetism at room temperature using an electric field. *Nature* **516,** 370-373 (2014).

[39] Saenrang, W. et al. Deterministic and robust room-temperature exchange coupling in monodomain multiferroic BiFeO$_3$ heterostructures. *Nature Communications* **8,** 1583-1590 (2017).

[40] Bibes, M. & Barthelemy, A. Towards a magnetoelectric memory. *Nature Materials* **7,** 425-426 (2008).

[41] Hu, J. M., Li, Z., Chen, L.Q. & Nan, C. W. High-density magnetoresistive random access memory operating at ultralow voltage at room temperature. *Nature Communications* **2,** 553-560 (2011).

[42] Heron, J. T., Schlom, D. G. & Ramesh, R. Electric field control of magnetism using BiFeO$_3$-based heterostructures. *Applied Physics Reviews* **1,** 021303 (2014).

[43] Fang, F., Yang, W., Zhang, F. C. & Luo, H. S. Fatigue Crack Growth for BaTiO3 Ferroelectric Single Crystals Under Cyclic Electric Loading. *J. Am. Ceram. Soc.*, **88,** 2491-2497 (2005).

[44] Park, S. E. & Shrout, T. R. Ultrahigh strain and piezoelectric behavior in relaxor based ferroelectric single crystals. *J. Appl. Phys.* **82,** 1804-1811 (1997).

[45] Viehland, D. & Salje, E. K. H. Domain boundary-dominated systems: adaptive structures and functional twin boundaries. *Advances in Physics*, **63,** 267-326 (2014).

[46] Wu, T. et al. Domain engineered switchable strain states in ferroelectric (011) [Pb(Mg$_{1/3}$Nb$_{2/3}$)O$_3$]$_{(1-x)}$-[PbTiO$_3$]$_x$(PMN-PT, x≈0.32) single crystals. *J. Appl. Phys.* **109**, 124101 (2011).

[47] Wang, Z., Wang, Y., Ge, W., Li, J. & Viehland, D. Volatile and nonvolatile magnetic easy-axisrotation in epitaxial ferromagnetic thin films on ferroelectric single crystal substrates. *Appl. Phys. Lett*. **103,** 132909 (2013).

[48] Liu, M. et al. Voltage-Impulse-Induced Non-Volatile Ferroelastic Switching of Ferromagnetic Resonance for Reconfigurable Magnetoelectric Microwave Devices. *Adv. Mater.* **25,** 4886-4892 (2013).

[49] Zhang, S. et al. Giant electrical modulation of magnetization in Co$_{40}$Fe$_{40}$B$_{20}$/Pb(Mg$_{1/3}$Nb$_{2/3}$)$_{0.7}$Ti$_{0.3}$O$_3$(011) heterostructure. *Sci. Rep.* **4**, 3727-3733 (2014).

[50] Heidler, J. et al. Manipulating magnetism in La$_{0.7}$Sr$_{0.3}$MnO$_3$ via piezostrain. *Phys. Rev. B* **91,** 024406 (2015).

[51] Zhou, C., Wang, F., Dunzhu, G., Yao, J. & Jiang, C. Piezostrain tuning non-volatile 90° magnetic easy axis rotation in Co$_2$FeAl Heusler alloy film grown on Pb(Mg$_{1/3}$Nb$_{2/3}$)O$_3$-PbTiO$_3$ heterostructures. *J. Phys. D: Appl. Phys.* **49,** 455001 (2016).

[52] Noheda, B., Cox, D. E., Shirane, G., Gao, J., & Ye, Z.-G. Phase diagram of the ferroelectric relaxor (1-x)PbMg$_{1/3}$Nb$_{2/3}$O$_3$-xPbTiO$_3$. *Phys. Rev. B* **66,** 054104 (2002).

[53] Peng, J. et al. Shear-mode piezoelectric properties of 0.69Pb(Mg$_{1/3}$Nb$_{2/3}$)O$_3$-0.31PbTiO$_3$ single crystals. *Solid State Commun.* **130,** 53-57 (2004).

[54] Pertsev, N. A. Giant magnetoelectric effect via strain-induced spin reorientation transitions in ferromagnetic films. *Phys. Rev. B* **78,** 212102 (2008).

Methods

Sample fabrication. We used room-temperature e-beam assisted evaporation with a base pressure of 1.5×10^{-10} mbar to deposit 10 nm of polycrystalline Ni at ~0.4 nm min^{-1}, and a 3 nm Cu cap against oxidation, on two unpoled substrates of PMN-PT ($x = 0.32$) $(011)_{pc}$ from Atom Optics. For each sample, the Cu/Ni bilayer served as the top electrode, and we sputter-deposited a back electrode of Pt. The $x \parallel [100]_c$ and $y \parallel [0\bar{1}1]_c$ axes (Fig. 1) along substrate edges were identified using x-ray diffraction, which we performed using a four-circle high-resolution Panalytical Empyrean vertical diffractometer.

Sample history. After poling, Sample 1 was electrically cycled while obtaining PEEM data (Fig. 3), and then electrically and magnetically cycled while making macroscopic magnetic measurements (Figs 2,3). Sample 2 was used only to investigate the magnetic anisotropy of the electrically virgin state (Supplementary Note 1).

Macroscopic magnetic measurements. We used a Princeton Measurements Corporation vibrating sample magnetometer with a bespoke probe[21] whose wiring permitted the application of electric fields.

Magnetic vector maps. Raw images were obtained in zero applied magnetic field on beamline I06 at Diamond Light Source, where we used an Elmitec SPELEEM-III microscope to map secondary-electron emission arising from circularly polarized x-rays that were incident on the sample surface at a grazing angle of 16°. The probe depth was ~7 nm, and the lateral resolution in our 50 μm-diameter field of view was typically ~135 nm (corresponding to pixels that represent ~49 nm). A 300 V power supply was connected to the top and bottom electrodes via feedthroughs in the sample holder.

Raw images were acquired during 1 s exposure times with right (R) and left (L) circularly polarized light, both on the Ni L_3 resonance at 851 eV, and off this resonance at 842 eV. The pixels in a raw XMCD-PEEM image describe the XMCD asymmetry $\left(I^R - I^L\right)/\left(I^R + I^L\right)$, which represents the projection of the local surface magnetization on the incident-beam direction. Here, $I^{R/L} = \left(I^{R/L}_{on} - I^{R/L}_{off}\right)/I^{R/L}_{off}$ denotes the relative intensity for secondary electron emission due to x-ray

absorption on ($I_{\mathrm{on}}^{\mathrm{R/L}}$) and off ($I_{\mathrm{off}}^{\mathrm{R/L}}$) the Ni L_3 resonance (the comparison between intensities obtained on and off resonance avoids the influence of any inhomogeneous illumination).

We averaged 100 raw XMCD-PEEM images to obtain a single XMCD-PEEM image for each of two orthogonal sample orientations. These two images were combined in order to yield vector maps of in-plane magnetization, after correcting for drift and distortion via an affine transformation that was based on topographical images of x-ray absorption for each sample orientation. Each of these topographical images was obtained by averaging all raw images that had been obtained on resonance with left and right-polarized light.

Supplementary information

for

Shear-strain mediated magnetoelectric effects revealed by imaging

M. Ghidini[1,2,3*], R. Mansell[4], F. Maccherozzi[2], X. Moya[3], L. C. Phillips[3], W. Yan[3], D. Pesquera[3], C. H. W. Barnes[4], R. P. Cowburn[4], J.-M. Hu[5], S. S. Dhesi[2‡] and N. D. Mathur[3†]

[1] Department of Mathematics, Physics and Computer Science, University of Parma, 43124 Parma, Italy.

[2] Diamond Light Source, Chilton, Didcot, Oxfordshire, OX11 0DE, UK.

[3] Department of Materials Science, University of Cambridge, Cambridge, CB3 0FS, UK.

[4] Cavendish Laboratory, University of Cambridge, CB3 0HE, UK.

[5] Department of Materials Science and Engineering, University of Wisconsin–Madison, Madison, Wisconsin 53706, USA.

* massimo.ghidini@unipr.it

‡ dhesi@diamond.ac.uk

† ndm12@cam.ac.uk

Contents

Supplementary Note 1

The effect of poling on in-plane magnetic anisotropy

(A) Absence of in-plane magnetic anisotropy before poling. The electrically virgin state of Ni//PMN-PT $(011)_{pc}$ shows no in-plane magnetic anisotropy, as seen from the macroscopic measurements presented below. This absence of anisotropy is consistent with our observation that the XMCD-PEEM vector map of a small area in the virgin sample (bottom-right inset, Fig. S1) differs substantially with respect to all XMCD-PEEM vector maps obtained after poling (Fig. 3b,e,h in the main paper).
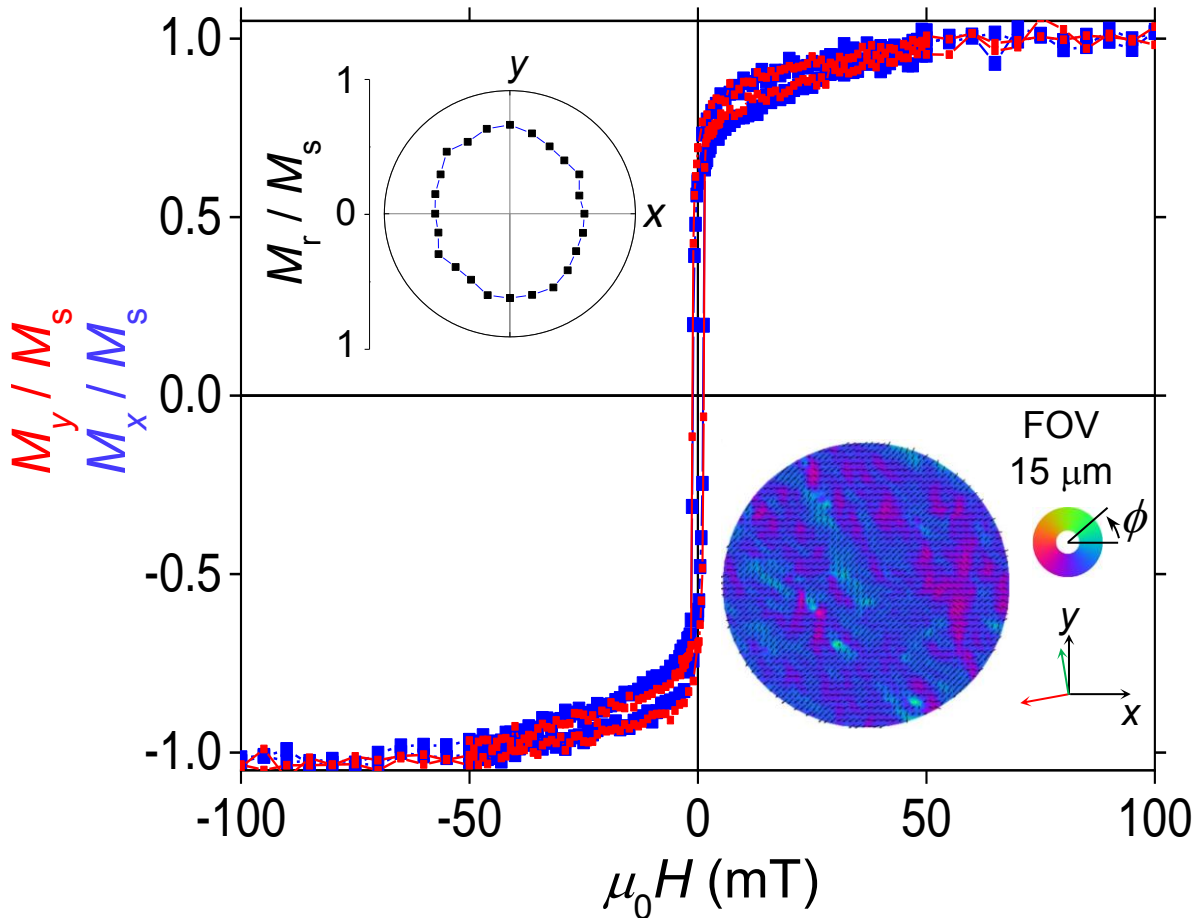
Figure S1. Magnetic measurements in electrically virgin Ni//PMN-PT $(011)_{pc}$. Reduced magnetization components M_y/M_s (red) and M_x/M_s (blue) versus applied collinear magnetic field H, where M_s denotes saturation magnetization. Upper-left inset: polar plots of squareness M_r/M_s derived from plots that include those shown in the main figure, where M_r denotes remanent magnetization. Lower-right inset: 15 µm-diameter XMCD-PEEM vector map of in-plane magnetization direction ϕ for the virgin sample. Green and red arrows denote in-plane projections of the grazing-incidence x-ray beam. All data recorded on Sample 2.

(B) In-plane magnetic anisotropy after poling. After poling the substrate by applying and removing an electric field of $E = -1$ MV m^{-1} along $+z$ (Fig. 1 in the main paper), Ni//PMN-PT (011)$_{pc}$ developed uniaxial magnetic anisotropy with the easy axis along y and the hard axis along x (Fig. 3a in the main paper). To identify the magnitude of this anisotropy, we obtained 'virgin' magnetization measurements along x and y after having performed a.c. demagnetization along each of these directions (Fig. S2). The difference in the areas under the two curves corresponds to a magnetic anisotropy energy of $E_a = 40$ kJ m^{-3}, which we identify to be $|\frac{3}{2}\sigma\lambda|$ given a magnetic stress anisotropy of $-\frac{3}{2}\sigma\lambda_s\cos^2(\theta)$ for orthogonal in-plane directions θ. This identification implies a stress $\sigma = E_Y\varepsilon$ that corresponds to a strain of $\varepsilon \sim 0.08\%$, consistent with the compressive strain of this magnitude that was measured along y (ref. 26 in the main paper). [For room-temperature Ni, we assume saturation magnetostriction $\lambda_s = -32.9\times10^{-6}$ and Young's modulus $E_Y = 133$ GPa.]
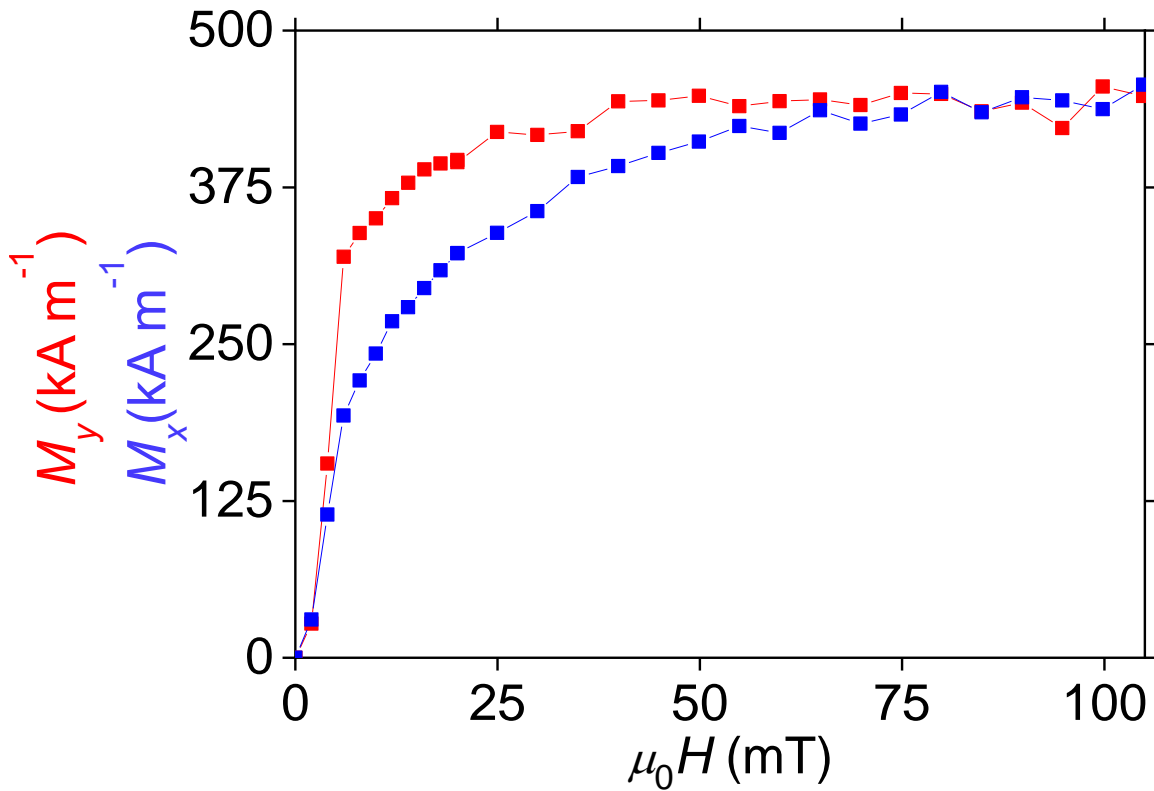

Figure S2. 'Virgin' magnetization measurements of Ni//PMN-PT (011)$_{pc}$ at zero electric field after poling. Magnetization components M_y (red) and M_x (blue) versus applied collinear magnetic field H. Each plot was obtained after a.c. demagnetization. All data recorded on Sample 1.

Macroscopic ME effects measured along x

Here we present macroscopic ME data measured along x, to complement the macroscopic ME data measured along y (Fig. 2 in the main paper).
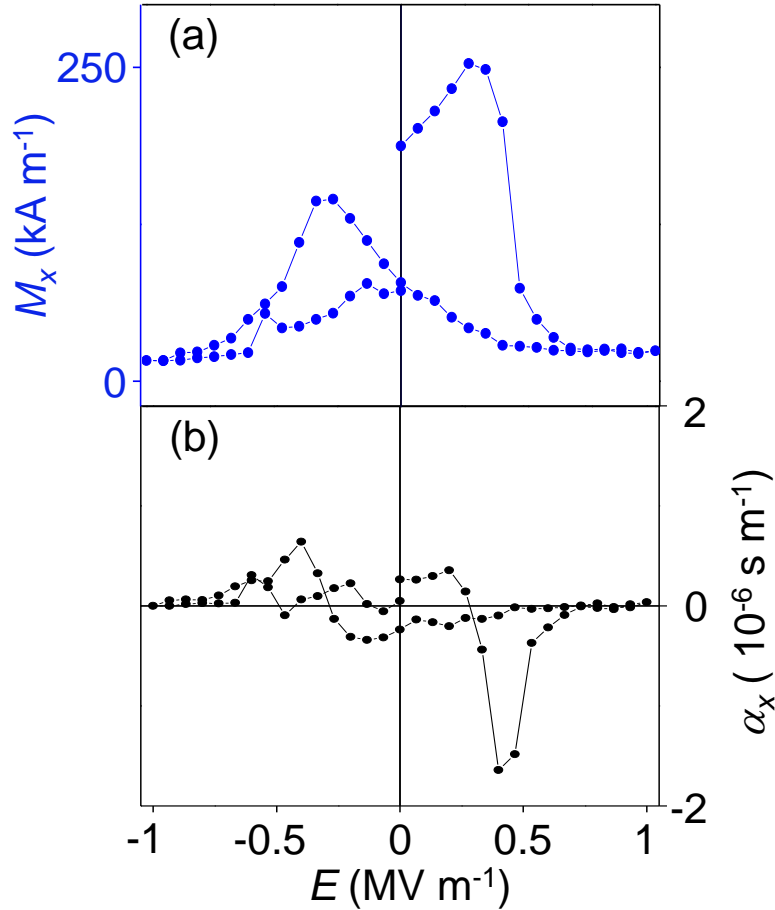

Figure S3. Macroscopic ME effects in Ni//PMN-PT (011)$_{pc}$. (a) In-plane magnetization component M_x versus electric field E applied perpendicular to the film plane. Hence (b) ME coupling coefficient $\alpha_x = \mu_0 dM_x/dE$. Data recorded on Sample 1, acquired directly after acquiring the corresponding plot of $M_y(E)$ (Fig. 2 in the main paper).

Ferroelectric polarization and macroscopic strain in PMN-PT (011)$_{pc}$

The electrically driven magnetic changes in Ni//PMN-PT (011)$_{pc}$ (red data in Fig. S4a, copied from Fig. 2a of the main paper) display extrema near the PMN-PT coercive fields of ±0.37 MV m^{-1} (blue data in Fig. S4a) and the extrema of macroscopic strain (Fig. S4b).
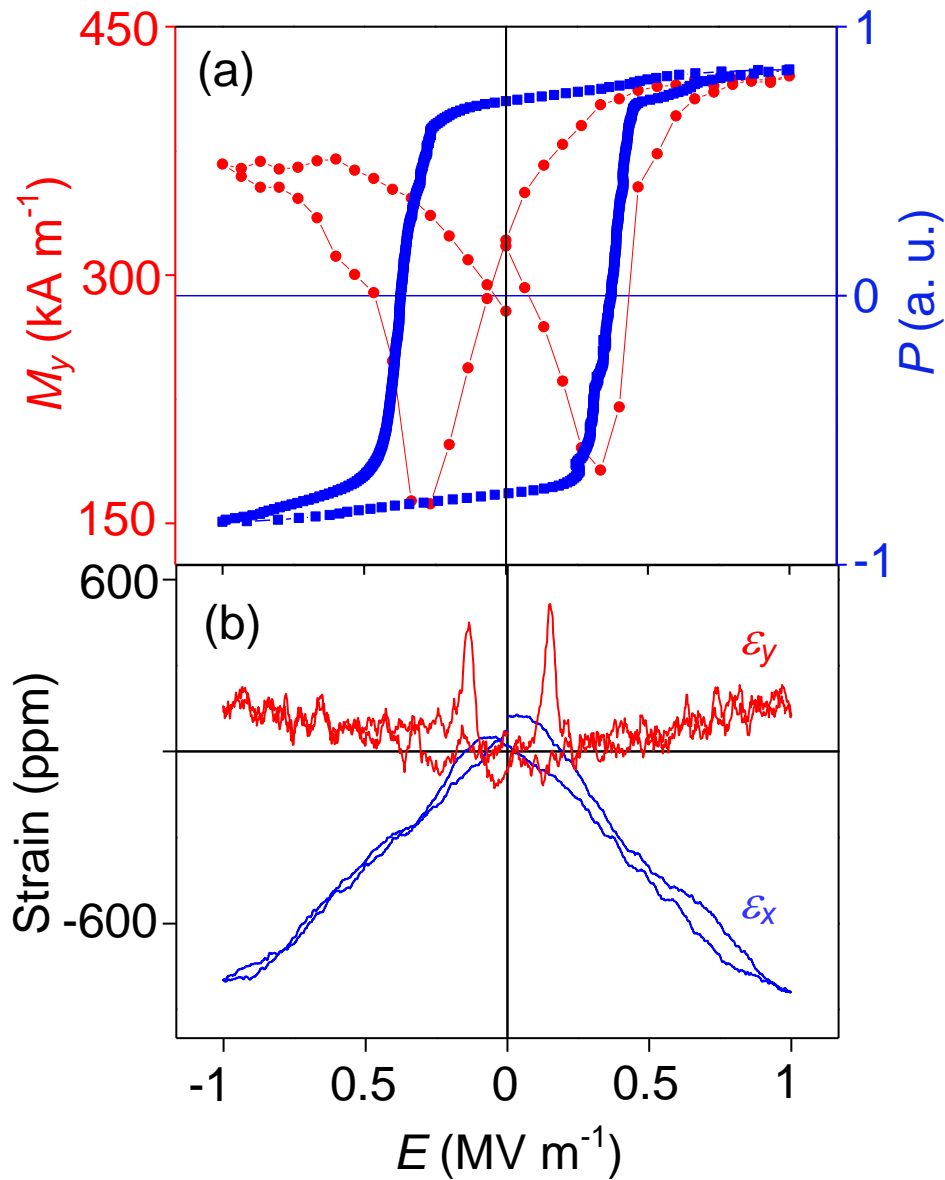
Figure S4. Ferroelectric polarization and macroscopic strain in PMN-PT (011)$_{pc}$. (a) Polarization P (blue) and (b) in-plane strain components ε_x (blue) and ε_y (red) versus electric field E. In (a) we reproduce $M_y(E)$ (red) from Fig. 2a in the main paper. Data in (a) recorded on Sample 1, data in (b) recorded on a PMN-PT substrate from the same batch.

Supplementary Note 4

Normal and shear strains due to ferroelectric domain switching in PMN-PT (011)$_{pc}$

Here we calculate the effect of ferroelectric domain switching on quadrants of the pseudocubic unit cell ($a = 4.017$ Å and $\theta = 89.89°$ from ref. 52 in the main paper) for rhombohedral PMN-PT. We will consider positive shear only, given that negative shear is analogous. **In all of the text and all of the figure that we show in this Note, all vectors are given for the pseudocubic unit cell with polarization $P_1^{\pm}$, and the pc subscript is dropped for simplicity.** Distances and angles in the pseudocubic unit cell with polarization $P_3^{\pm}$ are identified by recognizing that sheared quadrants in the vertical x-z plane of the pseudocubic unit cell for $P_1^{\pm}$ are equivalent to sheared quadrants in the horizontal x-y plane of the pseudocubic unit cell for $P_3^{\pm}$. This equivalence avoids fresh crystallographic notation.

The distortion switches with the polarization as follows:
- $P_1^{\pm}$ in the vertical x-z plane implies that quadrants in this plane are distorted (blue, Fig. S5a), and quadrants in the horizontal x-y plane are undistorted (green, Fig. S5b,c).
- $P_3^{\pm}$ in the horizontal x-y plane implies that quadrants in this plane are distorted (blue, Fig. S5b,d), and quadrants in the vertical x-z plane are undistorted (green, Fig. S5a).
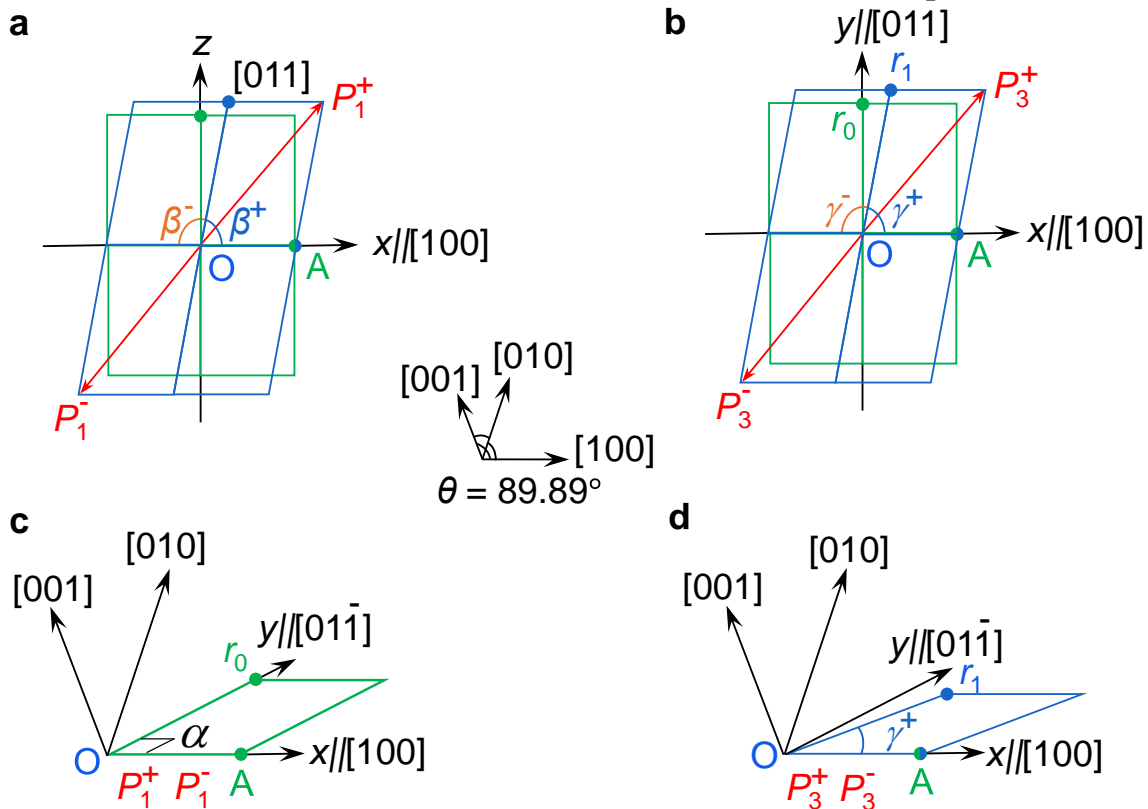
Fig. S5. The normal and shear strains arising from domain switching in the pseudocubic unit cell of PMN-PT. In (a) the vertical x-z plane, and (b-d) the horizontal x-y plane, which we show in (a,b) plan view and (c,d) perspective, quadrants are distorted (blue) when the polarization (red arrows) lies in the same plane, and quadrants are undistorted (green) when the polarization lies in the other of the two planes. All of the basis (and related) vectors that we specify are given for the pseudocubic unit cell with polarization $P_1^{\pm}$.

The distortion in both of the *x-y* and *x-z* planes is equivalent. We will calculate it below for the horizontal *x-y* plane of the film (Fig. S5a-d):

- The pseudocubic unit cell parameters for PMN-PT are a = 4.017 Å and θ = 89.89° (ref. 52 in the main paper).

- The distortion does not modify point A at (x_A, y_A), where $x_A = a/2$ and $y_A = 0$.

- The distortion translates point r_0 at (x_0, y_0) to r_1 at (x_1, y_1).

- Point r_0 at (x_0, y_0) is identified for the unit cell with polarization $P_1^{\pm}$:

  o [01$\bar{1}$] and [100] are separated by $\alpha = \cos^{-1}\left[\frac{[01\bar{1}]\cdot[100]}{|01\bar{1}|\cdot|100|}\right] = \cos^{-1}\left[\frac{([010]+[00\bar{1}])\cdot[100]}{|01\bar{1}|\cdot|100|}\right]$

  $$= \cos^{-1}\left[\frac{[010]\cdot[100]+[00\bar{1}]\cdot[100]}{|01\bar{1}|\cdot|100|}\right]$$

  $$= \cos^{-1}\left[\frac{a^2\cos\theta + a^2\cos(180° - \theta)}{|01\bar{1}|\cdot|100|}\right]$$

  $$= \cos^{-1}\left[\frac{0}{|01\bar{1}|\cdot|100|}\right] = 90°$$

  o $x_0 = 0$

  o $y_0 = |01\bar{1}|/2 = 0.5\sqrt{([010]+[00\bar{1}])^2} = 0.5\sqrt{a^2+a^2+2a^2\cos(180° - \theta)}$

  $$= 0.5a\sqrt{2+2\cos(180° - \theta)} \sim 2.83772 \text{ Å}$$

- Point r_1 at (x_1, y_1) is identified for the unit cell with polarization $P_3^{\pm}$:

  o $x_1 = |Or_1|\cos\gamma^+$ and $y_1 = |Or_1|\sin\gamma^+$

  o The distorted quadrant with polarization $P_3^{\pm}$ in the *x-y* plane is equivalent to the distorted quadrant with polarization $P_1^{\pm}$ in the *x-z* plane, for which we wrote the crystallographic notation used throughout this Supplementary Note, including Fig. S5a-d.

  o To avoid introducing a second set of crystallographic notation when polarization $P_3^{\pm}$ lies in the *x-y* plane, distance $|Or_1|$ and angle γ^+ will be evaluated by setting them equal to the distance $|011|$ and angle β^+ for the distorted quadrant with polarization $P_1^{\pm}$ in the *x-z* plane. This equivalence permits us to write:

    ▪ $|Or_1| = 0.5|011| = 0.5a\sqrt{2+2\cos\theta} \sim 2.8431733$ Å.

    ▪ $\gamma^+ = \beta^+ = \cos^{-1}\left[\frac{[011]\cdot[100]}{|011|\cdot|100|}\right] = \cos^{-1}\left[\frac{([010]+[001])\cdot[100]}{|011|\cdot|100|}\right] = \cos^{-1}\left[\frac{[010]\cdot[100]+[001]\cdot[100]}{|011|\cdot|100|}\right]$

    $$= \cos^{-1}\left[\frac{2a^2\cos\theta}{a^2\sqrt{2+2\cos\theta}}\right] = \cos^{-1}\left[\frac{2\cos\theta}{\sqrt{2+2\cos\theta}}\right] \sim 89.84°.$$

    … such that $x_1 = |Or_1|\cos\gamma^+ \sim 0.007712$ Å and $y_1 = |Or_1|\sin\gamma^+ \sim 2.843163$ Å.

- When the polarization switches from $P_1^{\pm}$ in the *x-z* plane to $P_3^{\pm}$ in the *x-y* plane:

  o Normal strain $\varepsilon_{yy} = \frac{y_1 - y_0}{y_0} \sim 0.1918\%$

  o Normal strain $\varepsilon_{xx} = \frac{x_A - x_A}{x_A} = 0$

  o Shear strain $\varepsilon_{xy} = \varepsilon_{yx} = \frac{1}{2}\left(\frac{x_1 - x_0}{y_0} + \frac{0}{x_A}\right) \sim 0.1359\%$

Supplementary Note 5
Principal axes of strain from the Mohr's circle construction

Unit-cell quadrants in our PMN-PT $(011)_{pc}$ substrate undergo both normal and shear strains when the polarization switches to lie in the plane of any such quadrants (Supplementary Note 4). Here we show that the corresponding principal axes of strain lie at 27.4° with respect to the Cartesian basis vectors, and that the normal strains in the rotated basis are -0.07% and +0.26%. Our analysis is performed for the *x-y* surface plane of interest, while a similar analysis would hold for the *x-z* vertical plane.

As shown in Supplementary Note 4, when the polarization switches to lie in the *x-y* surface plane, a normal strain ($\varepsilon_{yy} = 0.1918\%$ and $\varepsilon_{xx} = 0$) is accompanied by a shear strain that can be positive ($\varepsilon_{xy} = 0.1359\%$ for $P_{1,2}^{\pm} \rightarrow P_3^{\pm}$) or negative ($\varepsilon_{xy} = $ -0.1359% for $P_{1,2}^{\pm} \rightarrow P_4^{\pm}$). For both scenarios (Fig. S6a,b), we first identify points R($\varepsilon_{yy}, \varepsilon_{xy}$) and T($0, -\varepsilon_{xy}$) on diametrically opposite sides of Mohr's circle[S1] [centre C($\frac{\varepsilon_{yy}}{2}, 0$), radius $r = \sqrt{\frac{\varepsilon_{yy}^2}{4} + \varepsilon_{xy}^2}$]. We then rotate the coordinate system by $\phi = -\theta = \frac{1}{2}\tan^{-1}(\frac{2\varepsilon_{xy}}{\varepsilon_{yy}})$ to yield new principal axes x' and y', with $\phi = $ -27.4° for positive shear (Fig. S7a), and $\phi = $ 27.4° for negative shear (Fig. S7b). In this new coordinate system, there is no shear strain, and normal strains of $\varepsilon_{xx}' = \frac{\varepsilon_{yy}}{2} - r = $ -0.07% and $\varepsilon_{yy}' = \frac{\varepsilon_{yy}}{2} + r = $ +0.26% are identified via $S_1(\varepsilon_{xx}', 0)$ and $S_2(\varepsilon_{yy}', 0)$ in Fig. S6a,b. In hitherto unstrained regions of our negative-magnetostriction Ni film, these normal strains yielded magnetic easy axes along x', and magnetic hard axes along y'.

(a) $\varepsilon_{xy} > 0$ (b) $\varepsilon_{xy} < 0$
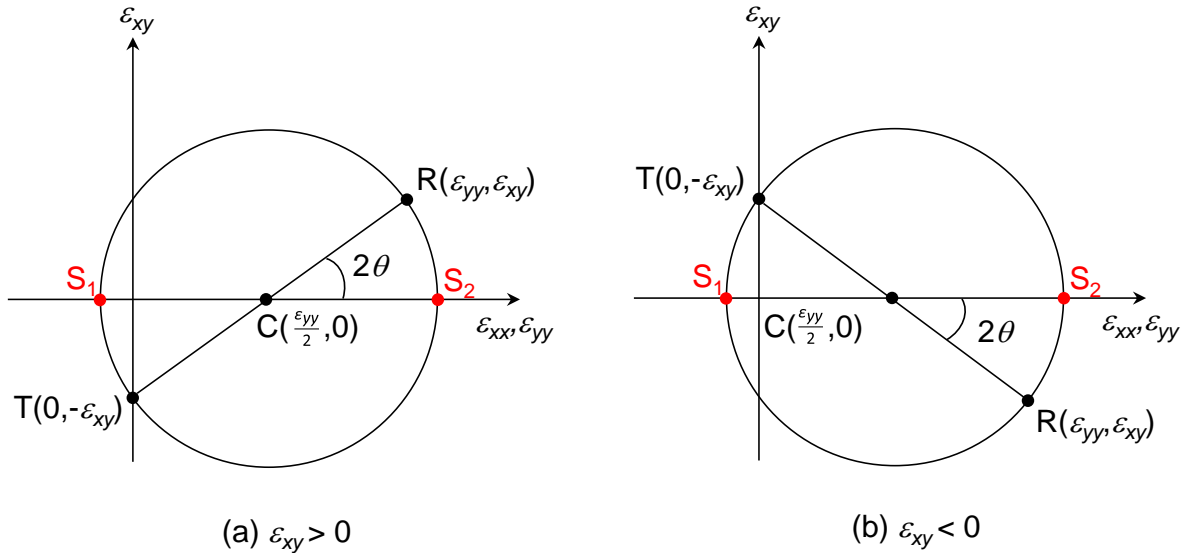
Fig. S6. The Mohr's circle construction. (a) Positive shear strain $\varepsilon_{xy} > 0$ implies $\theta > 0$. (b) Negative shear strain $\varepsilon_{xy} < 0$ implies $\theta < 0$. Points $S_1(\varepsilon_{xx}', 0)$ and $S_2(\varepsilon_{yy}', 0)$ were used to identify normal strains ε_{xx}' and ε_{yy}' along new principal axes x' and y', which are rotated by $\phi = -\theta = $ -27.4° with respect to *x* and *y*, as shown in Fig. S7a,b.
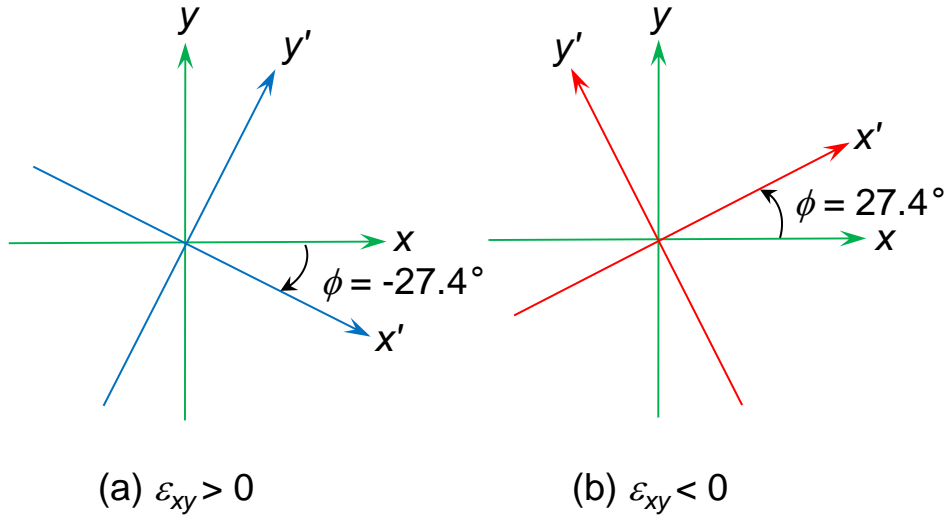
Fig. S7. New principal axes of strain and the resulting magnetic easy axes. (a) Positive shear strain $\varepsilon_{xy} = 0.1359\%$ and normal strain $\varepsilon_{yy} = 0.1918\%$ correspond to normal strains of $\varepsilon'_{xx} = -0.07\%$ and $\varepsilon'_{yy} = +0.26\%$ along new principal axes x' and y', which are rotated by $\phi = -\theta = -27.4°$ with respect to x and y. The resulting magnetic easy axis lies along x' and thus at $+62.6°$ to y, while the resuling magnetic hard axis lies along y' and thus at $+62.6°$ to x. (b) Negative shear strain $\varepsilon_{xy} = -0.1359\%$ and normal strain $\varepsilon_{yy} = 0.1918\%$ correspond to normal strains of $\varepsilon'_{xx} = -0.07\%$ and $\varepsilon'_{yy} = +0.26\%$ along new principal axes x' and y', which are rotated by $\phi = -\theta = 27.4°$ with respect to x and y. The resulting magnetic easy axis lies along x' and thus at $-62.6°$ to y, while the resuling magnetic hard axis lies along y' and thus at $-62.6°$ to x.

[S1] J. F. Nye, *Physical properties of crystals*, Oxford University Press (1957), pages 43-46.

<div align="center">

Supplementary Note 6

A and B regions in the magnetic vector maps at $E_{1,2,3}$

</div>

The four steps below (summarized in Table S1, overleaf) describe our magnetic vector maps (Fig. 3b,e,h in the main paper) in terms of ferroelectric domain polarizations (Fig. 6a-e in the main paper).

After growth. We assume that the unpoled substrate contained a mixture of $P_{3,4}^{\pm}$ domains (whose polarizations lay in the *x-y* plane) and $P_{1,2}^{\pm}$ domains (whose polarizations lay away from the *x-y* plane). Regions of the film that grew on $P_{3,4}^{\pm}$ domains are labelled A. Regions of the film that grew on $P_{1,2}^{\pm}$ domains are labelled B. We assume zero growth strain because the film was very thin (10 nm) and possessed no in-plane magnetic anisotropy (Supplementary Note 1).

$E_1 = 0$ after poling. All ferroelectric domain polarizations lay down with respect to the *x-y* plane, and film magnetization was nominally aligned along $\pm y$ (Fig. 3b) as expected (ref. 26 in the main paper). The A regions developed magnetic easy axes along *y* (vertical grey arrow, Fig. 6f) because the underlying ferroelectric domain polarizations imparted compressive strain along *y* when switching down from the *x-y* plane (the absence of shear is attributed to clamping by the intervening ferroelectric domains, which underwent no net change of strain). Unstrained B regions lying above these intervening ferroelectric domains were exchange coupled to the newly strained A regions. Therefore the local magnetization was nominally aligned along $\pm y$ at all locations away from magnetic domain walls (Fig. 3b).

$E_1 \rightarrow E_2$. All ferroelectric domain polarizations switched into the *x-y* plane. Hitherto unstrained B regions developed local magnetizations at nominally $\pm 62.6°$ to $\pm y$ because magnetic easy axes were created along these directions (non-vertical grey arrows, Fig. 6f) when the underlying ferroelectric domain polarizations switched into the *x-y* plane. Newly unstrained A regions, whose underlying ferroelectric domain polarizations had returned to the *x-y* plane, were exchange coupled to the newly strained B regions, such that magnetic domains were typically larger than the ~300 nm lower bound on ferroelectric domain size[45] (Fig. 3e).

$E_2 \rightarrow E_3$. All ferroelectric domain polarizations switched up from the x-y plane, thus reversing the changes of strain in the x-y plane that occurred during the previous field step. The magnetic easy axis along $\pm y$ was therefore restored in re-strained A regions (vertical grey arrow, Fig. 6f), and newly unstrained B regions were exchange coupled to these re-strained A regions. Therefore the local magnetization was nominally aligned along $\pm y$ at all locations away from magnetic domain walls (Fig. 3h). The magnetic domain configuration at E_1 was recovered with good fidelity at E_3 because sub-90° magnetic rotations preserved the sign of the y-axis component of local magnetization. An immediate consequence of this preservation is that some magnetic domain walls common to E_1 and E_3 can just be discerned at E_2.

Electrical state	A regions	B regions
$P_{3,4}^{\pm}$ domains under A regions after growth $P_{1,2}^{\pm}$ domains under B regions after growth	No film strain EC to B regions $\mathbf{M}/\lvert\mathbf{M}\rvert$ undefined	No film strain EC to A regions $\mathbf{M}/\lvert\mathbf{M}\rvert$ undefined
$P_{1,2}^{-}$ domains under A and B regions at E_1	Film strain EA along $\pm y$ $\mathbf{M}$ along $\pm y$	No film strain EC to A regions $\mathbf{M}$ along $\pm y$
$P_{3,4}^{\pm}$ domains under A and B regions at E_2	No film strain EC to B regions $\mathbf{M}$ at $\pm 62.6°$ to y	Film strain EA at $\pm 62.6°$ to y $\mathbf{M}$ at $\pm 62.6°$ to y
$P_{1,2}^{+}$ domains under A and B regions at E_3	Film strain EA along $\pm y$ $\mathbf{M}$ along $\pm y$	No film strain EC to A regions $\mathbf{M}$ along $\pm y$

Table S1. Summary of the ME switching in Ni//PMN-PT (011)$_{\mathbf{pc}}$. For each stage in the electrical history of our magnetically virgin sample, we specify the ferroelectric domain species expected to lie directly below A and B regions of the film, whose local magnetization is denoted $\mathbf{M}$. Strained regions displayed uniaxial anisotropy (Fig. 6f), with the easy axis (EA) predicted to lie along y at E_1 and E_3, and at $\pm 62.6°$ to y at E_2 (+62.6° for positive shear, -62.6° for negative shear). Unstrained regions were exchange coupled (EC) to strained regions, with any conflicts resolved by the presence of magnetic domain walls.